Nanotechnology

PAPER

Probing electromechanical behaviors by datacube piezoresponse force microscopy in ambient and aqueous environments

To cite this article: Anyang Cui *et al* 2019 *Nanotechnology* **30** 235701

IOP Publishing Nanotechnology
Nanotechnology 30 (2019) 235701 (10pp) https://doi.org/10.1088/1361-6528/ab0866

Probing electromechanical behaviors by datacube piezoresponse force microscopy in ambient and aqueous environments

Anyang Cui[1,5], Peter De Wolf[2,5], Yan Ye[1], Zhigao Hu[1,3], Antoine Dujardin[2,4], Zhuangqun Huang[2], Kai Jiang[1], Liyan Shang[1], Ming Ye[2], Hao Sun[2] and Junhao Chu[1]

[1] Key Laboratory of Polar Materials and Devices (MOE) and Technical Center for Multifunctional Magneto-Optical Spectroscopy (Shanghai), Department of Electronic Engineering, East China Normal University, Shanghai 200241, People's Republic of China
[2] Bruker Nano Surfaces, Santa Barbara, California, CA 93117, United States of America
[3] Collaborative Innovation Center of Extreme Optics, Shanxi University, Taiyuan, Shanxi 030006, People's Republic of China
[4] Cellular Microbiology and Physics of Infection Group—Lille Centre for Infection and Immunity, CNRS UMR8204, INSERM U1019, Lille Regional Hospital University Centre, University of Lille, Institut Pasteur de Lille, Lille F-59021, France

E-mail: zghu@ee.ecnu.edu.cn

Received 8 November 2018, revised 29 January 2019
Accepted for publication 19 February 2019
Published 21 March 2019

Abstract

For assisting the in-depth investigations of widespread electromechanical phenomena in functional materials, piezoresponse force microscopy (PFM) has gradually evolved to realize full information-flow acquisition and fit the conductive liquid working environments. Here, we designed data cube (DCUBE) based PFM to collect the electromechanical effect into a high-dimensional array of piezoresponse by adding *ac* bias with a wide range of frequencies to the probe. The electromechanical and mechanical spectra can be consecutively extracted at each pixel in the intermittent-contact mode. High-resolution ferroelectric domains of the poled $LiNbO_3$ were mapped, corresponding to the ideal phase contrasts of about 180° in air, decane, and deionized water. Rich information detection and non-contact mode in DCUBE-PFM bring many merits on the electromechanical characterizations, especially for elastic-inhomogeneous surfaces and soft materials. Moreover, we systematically reveal the Debye screening effect and time-resolved field-oriented ion dynamics, which play crucial roles in the reduction of PFM spatial resolution in electrolytes. These physical discussions provide strategies to further realize high-resolution electromechanical imaging in highly conductive liquid environments.

Supplementary material for this article is available online

Keywords: electromechanical behavior, DCUBE-PFM, conductive liquid, $LiNbO_3$

(Some figures may appear in colour only in the online journal)

1. Introduction

Local electromechanical activity is ubiquitous among ferroelectrics [1, 2], biological piezoelectric systems [3–6], macromolecules [7], and electrochemical applications [8–10]. Researchers have recently been looking for a reliable approach to directly observe the intrinsic electromechanical property in biological piezoelectric and mono/few-layer two-dimensional materials such as h-BN and 2H-MoS_2 [3, 4, 11, 12]. Piezoresponse force microscopy (PFM), as a

[5] These authors contributed equally to this work.

proven tool to map the electromechanical properties, has been continuously developed in past decades. In order to acquire the weak piezoelectric response ($d < 10\,\mathrm{pm\,V^{-1}}$) and control small excitations, the excited surface displacement can be observed at an adequate modulated frequency near the contact-resonance (CR) of the tip-surface junction. Based on CR-PFM, piezoelectric signals could be mapped with a reduced amplitude of modulation voltage, enabling detection of displacements down to the sub-pm range [13, 14]. However, the CR frequency is sensitive to the contact stiffness, which depends on the the surface morphology and local mechanical properties. This can give rise to topographic cross-talk superimposed onto the electromechanical images of interest. Typical multi-frequency PFM modes such as dual-frequency resonance-tracking and band excitation [15, 16], developed by Kalinin *et al*, show to improve the image resolution and avoid the resonant frequency shift error. Additionally, the non-contact mode PFM could lengthens lifetime of the tip and eliminates lateral forces, which is beneficial to characterize soft or fragile sample systems [17–20]. Therefore, further studies on PFM technique remains of strong interest, to make it into a generally applicable mode for improved piezoresponse detection, as well as multi-dimensional bulky data acquisition [18, 21–24].

Simultaneous imaging of local mechanical and piezoelectric properties is essential for the characterization of biological piezoelectricity and macromolecules [4–7]. On the other hand, the applications for energy storage, biofunctionality, and electroactive soft matter systems may require real-time nanoelectrical characterizations in a conductive liquid. The better control of tip-surface forces is an additional merit in liquid, where the detrimental impacts of both long-range electrostatic forces and capillary interactions in the ambient environment are mitigated. However, the transfer of the experimental setup from air to liquid phase is challenging, due to liquid conductivity, ion electromigration, and voltage-induced decomposition of many liquids. Some numerical models and physical mechanisms have been reported to reveal the electrical and mechanical field distribution around the tip-liquid-sample system [25–28]. Rodriguez and Balke *et al* have implemented a series of PFM work applied into distilled water and some electrolytes [17, 27–30]. These studies highlight the interests to improve PFM to satisfy the compatibility with conductive liquid environments, as well as to allow synchronous detection of local electromechanical and elastic properties.

Here, we developed the DCUBE-PFM mode based on the fast force volume (FFV) method to directly observe the resonance enhanced electromechanical activity on the nanoscale in the non-polar and polar solutions. Contact resonance enhanced piezoresponse and mechanical properties could be synchronously detected by employing FFV mode, which enables a faster, more accessible, easily implemented and robust means of nanoelectromechanical measurement. For antiparallel-polarized domains of ferroelectric poled $LiNbO_3$ crystal, ideal phase contrast of about 180° and enhanced piezoresponse can be acquired in air, decane, and deionized water (DI water). The spatial resolution in NaCl electrolytes was reduced with the molarity increasing. It could be systematically explained by the time-resolved ionic electromigration and electrical field screening effect. This work promotes the development of PFM technique and provides innovative strategies for high-resolution probing in conductive liquid environment.

2. Experimental section

The experiments in air, decane, DI water (Milli-Q Advantage) and NaCl solutions were carried out on the scanning probe microscopy (SPM) system (Dimension Icon, Bruker). The fully metal-coated conductive tip (SCM-PIT) was used to perform electromechanical imaging in decane. An additional type of the nanoelectrode tip (PFSECM) coated by SiO_2 layer was chosen for the electromechanical imaging in air, DI water and NaCl solutions of 1 and 10 mM. Tip of SCM-PIT is the common conductive probe, while another one has the insulated coating but a conductive tip apex. The Pt/Ir coating probe (SCM-PIT) holds a spring constant (k) of $\sim$2 N m^{-1}, and the resonant frequency of $\sim$68 kHz. For the pre-mounted nanoelectrode probe (PFSECM), the value of k is $\sim$1.5 N m^{-1}, and the resonant frequency is $\sim$62 kHz. The ramp rate in DCUBE-PFM mode is 30 Hz with the holding time of 100 ms. For electromechanical imaging in different working environments, the modulated voltage is set to make sure the better resolution of PFM amplitude and phase signals, as well as to be controlled to avoid the electrochemical reaction in polar solutions. Experiments were implemented on a standard periodically poled $LiNbO_3$ (PPLN) sample mounted on a metal sheet with poled domains of about 15 μm in width. The three-dimensional electromechanical data visualization was supported and processed by an open source program and Python package, Mayavi [31].

3. Results and discussion

3.1. DCUBE-PFM and 3D electromechanical data visualization

The DCUBE-PFM method images the electromechanical effect at a range of drive frequencies by combining FFV mode with the classic PFM technique. The former (FFV mode) efficiently controls the periodical motion of scanning probe to collect the topography and force–distance curve in each pixel of measured surface. The latter one (PFM) enables the tip to perceive the weak piezoresonse under the excitation voltage. Based on the inverse piezoelectric effect, PFM detects the bias induced picometer-scale surface deformation, where an *ac* voltage $V_{ac} = V_{dc} + V_0\cos(\omega t)$ is applied to a conductive tip [18, 32, 33]. The 'wave-shaped' scheme in figure 1(a) represents the motion locus of SPM tip during the force ramp in DCUBE-PFM imaging. DCUBE-PFM mode allows that the cantilever approaches the surface at each point in the image, then holds on the surface while the frequency is swept to collect the frequency dependent piezoresponse, and then the cantilever is retracted. Figure 1(b) illustrates the evolution

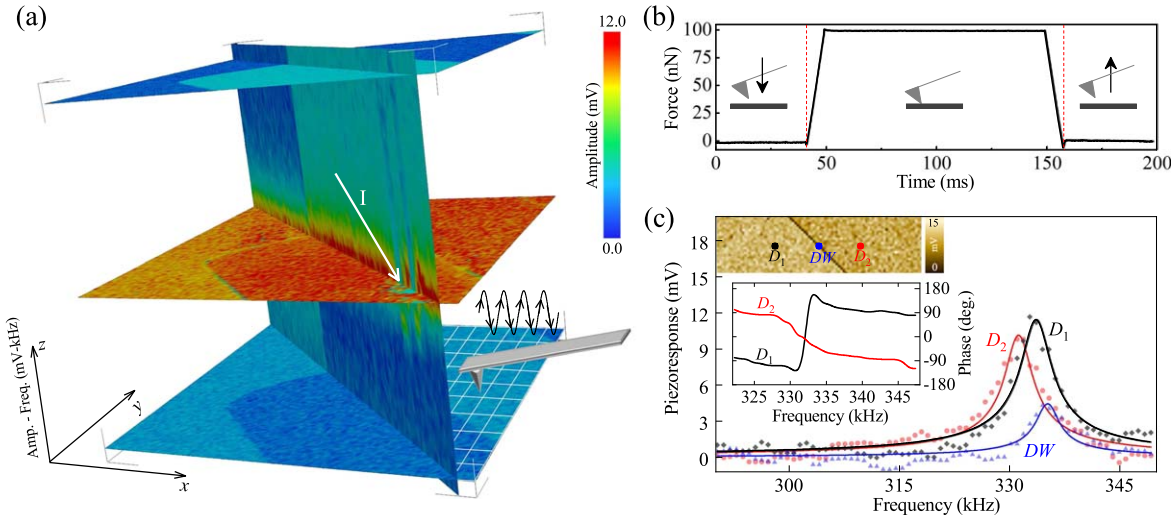

Figure 1. Three-dimensional visualization of amplitude, force distance spectrum in each pixel and the position-variant frequency spectra. (a) Three-dimensional data cube of piezoresponse amplitude imaged in air. The *x*–*y* plane presents the 30 μm by 30 μm scanning area. The axis *z* corresponds to the frequency-dependent piezoresponse amplitude (Amp.–Freq. curves) at the excitation frequency range of 300–370 kHz. Arrow *I* marks some surface features that are probably contaminants. At each pixel, the probe experiences the processes of approach, hold, and lift, as shown by the 'wave-shaped' scheme. The tip moves vertically with variable velocity modulated by the ramp voltage. (b) The force–distance curve between tip and surface in every ramp. (c) Original amplitude-frequency spectra (dot lines) and the fittings (solid lines) corresponding to the antiparallel domain regions (D_1, D_2) and a domain wall (*DW*), as marked in inset of the amplitude image. The accompanied phase behaviors (D_1, D_2) were plotted in the inset.

of the tip-surface force in every pixel. The tip approaches the surface vertically until the deflection setpoint is achieved. Next, the tip experiences a short period with a constant force, 100 nN in this work. The electromechanical data are collected in this dwell segment. After acquisition, the probe hops to the next position for the next detection, until a mesh of evenly-spaced M × N points are finished. One whole ramp process of 'approaching and retracting' motion could acquire the complete force–distance curve, which is a powerful tool to investigate the rich mechanical information of sample including the most commonly used quantities, such as elastic modulus, tip-sample adhesion, energy dissipation, and maximum deformation. The contact mode in traditional PFM is replaced by a hopping motion in DCUBE-PFM, which can efficiently eliminate the lateral forces.

In addition to the topographic height and force–distance relation, DCUBE-PFM method allows location (x, y) dependent and frequency (ω) dependent local electromechanical response to be obtained into a three-dimensional data cube $\{A, \varphi\}(x, y, \omega)$. As depicted in figure 1(a), 3D image shows a data cube of piezoresponse amplitude with 128 × 128 pixels. Frequency dependent piezoresponse $A(\omega)$ was extracted in each ramp process when tip touches the sample surface. Three amplitude planes parallel to the (x, y) scanning plane, captured at three drive frequencies of about 305, 330, and 365 kHz, respectively, are shown. The vertical plane parallel to the z axis maps the observed frequency-dependent amplitude from 300 to 370 kHz. By sliding the modulated frequency along the z axis, (see SI figure S1, Movie S1 and Movie S2 available online at stacks.iop.org/NANO/30/235701/mmedia) present the original 3D visualizations of amplitude and phase at every single drive frequency (see the supporting information).

During the dwell segment, the piezoresponse is detected by adding a drive excitation $V_{ac} = V_0 e^{i\omega t}$ to the tip. The V_{ac}-induced surface vibration, $u_{ac} = d_{33} V_0 e^{i\omega t + \varphi}$, of ferroelectric sample at every pixel can be acquired at a wide range of modulated frequencies (maximum range: 0.5 kHz–5 MHz), where d_{33} is the out-of-plane piezoelectric coefficient of sample, and φ is the phase contrast reflecting the ferroelectric polarized orientation. This surface vibration in turn drives the vibration of the cantilever that is in contact with the sample surface. The deflection of the cantilever induced by the piezoelectric response of the measured specimen is detected via the photodetector of AFM system. The cantilever deflection z meets the motion equation [34, 35]

$$\ddot{z} + \frac{\omega_0}{Q}\dot{z} + \omega_0^2 z = d_{33} V_0 e^{i(\omega t + \varphi)}, \tag{1}$$

where the quality factor Q is used to indicate the energy loss of the tip-surface system, and ω_0 is the resonant frequency of the harmonic oscillator. Under the circumstance, the frequency-dependent cantilever behavior can be given by using a simple harmonic oscillator model as follow

$$A(\omega) = \frac{d_{33} V_0 \omega_0^2}{\sqrt{(\omega_0^2 - \omega^2)^2 + (\omega\omega_0/Q)^2}}. \tag{2}$$

In terms of equation (2), the tip deflection is given by piezoresponse amplitude $A = d_{33} V_0$ when a quasi-static voltage is applied, while the tip deflection meets $A_0 = d_{33} V_0 Q$ magnified by Q factor if the modulation voltage is driven at the resonant frequency [34]. Moreover, it can be further seen that the measured piezoelectric coefficient d_{33} (pm V^{-1}) of material is proportional to the ratio of $\frac{A_0}{V_0 Q}$, as well as the *deflection sensitivity* (nm V^{-1}) of probe [36]. Experimentally, calculating d_{33} coefficient requires the precise calibration of

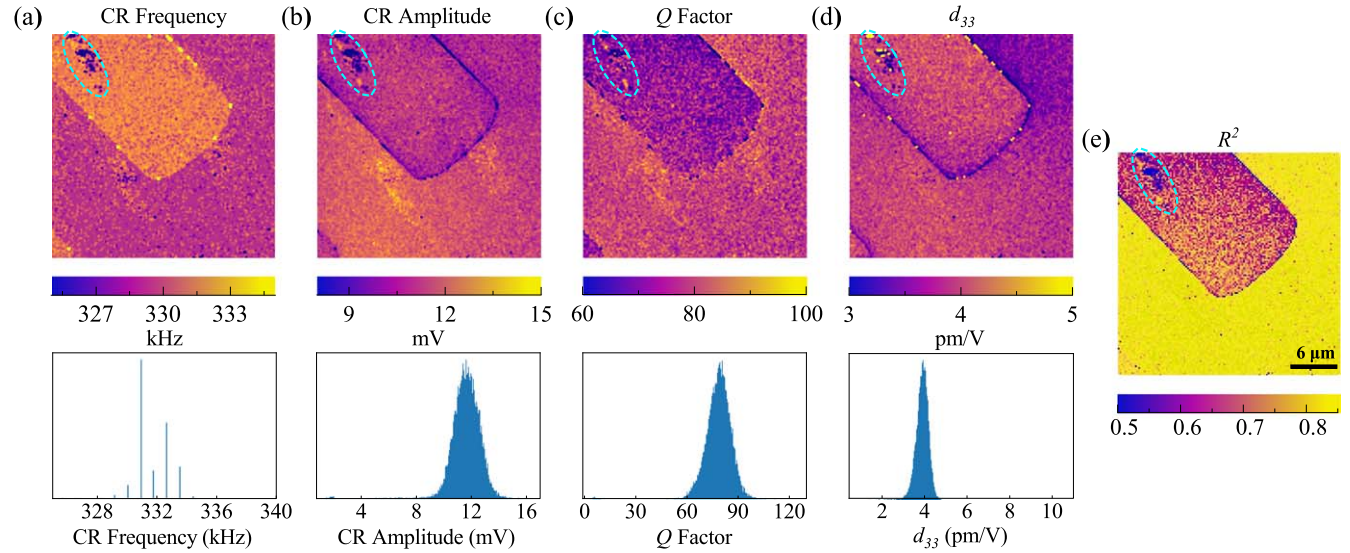

Figure 2. Quantification and visualization of piezoelectric response by the fitting process. In air, the mapping of (a) resonant frequency f_0, (b) resonance-enhanced amplitude A_0 at the contact resonance (CR), (c) quality factor Q, (d) the calculated d_{33} coefficient, and (e) the goodness of fit (R^2) for fitting amplitude-frequency curves using equation (2). Scale bar is set as 6 μm. The dashed ellipse marks residual surface features, which are probably contaminants. Beneath each image of panels (a)–(d), the statistic histogram was plotted to quantify the corresponding distribution of every signal.

probe's *deflection sensitivity* and Q factor, where in this work the *deflection sensitivity* of PFSECM probe was calibrated as 125 nm V^{-1}.

Frequency dependent piezoresponse, $A(\omega)$, in figure 1(c) was extracted from the 3D image of amplitude at antiparallel-polarized regions (D_1, D_2) and a domain wall (*DW*) as shown in inset of figure 1(c). The resonant peaks were fitted to equation (2). Significant reduction of peak intensity can be seen at the domain boundary. It exhibits excellent piezoresponse magnitudes at the center of the domain areas with the characteristic minima at the *DW*. In addition, the corresponding phase signals are opposed by about 180° for antiparallel polarizations, as plotted in the inset of figure 1(c).

The amplitude-frequency spectra at all measured pixels were fitted to quantify the CR peak position (ω_0, figure 2(a)) and piezoresponse (A_0, figure 2(b)) at contact resonance. The count distribution of each signal has been summarized as shown beneath the mapping panels in figures 2(a)–(d). The variation of resonant frequency is about 2 kHz between antiparallel domains in air. The CR amplitude illustrates that DCUBE-PFM can realize the electromechanical imaging with frequency-tracking of contact resonance, as well as can further summarize the Q factor and d_{33} coefficient at each pixel of sample surface. The mapping of Q factor in figure 2(c) shows the weak variation of the energy dissipation in cantilever-sample system at the different domains with antiparallel polarized directions. In terms of the applicable $LiNbO_3$ crystal after the poling process, it is difficult to make sure the perfectly uniform distribution of mechanical property in flat surface with the oppositely polarized lattice. It is accepted that the poling processing could change the physical and chemical properties such as lattice structure, stoichiometry, and surface charge differences of positively and negatively polarized surfaces in PPLN sample [37] It might result in a tiny shift of resonance frequency, slight difference in piezoresponse magnitude, and the various Q factor within the accepted experimental error range. After the known Q factor at each pixel and the probe calibration, d_{33} coefficient of the observed surface was calculated into figure 2(d). This d_{33} histogram mapping performs the uniform piezoelectric coefficient of the bulk PPLN single crystal, about 3.8 $\pm$ 0.8 pm V^{-1}.

Figure 2(e) illustrates a statistic distribution delineating pixels with the goodness of fit, R^2, corresponding to the fitting quality. The difference of R^2 between the antiparallel domain region is about 0.15, where the worse fitting results were ascribed to the poor symmetry of the resonant peak. Moreover, the dashed ellipses in figure 2 circle out the surface features that are probably contaminants, which have presented the differences in piezoelectric response compared to the base materials. The surface attachments of non-piezoelectric matters could not present frequency dependence of piezoresponse with very low amplitude and d_{33} value, corresponding to the bad performance of fitting. These suspicious surface contaminants are better visualized in figure 1(a) on the vertical spectral slice as pointed out by the arrow *I*.

3.2. Electromechanical visualization in liquids

The detection of electromechanical phenomena in liquids has been investigated on the PPLN sample through transferring the experimental system comprising tip holder and sample into a liquid cell. First, decane was selected, as one of the non-polar solutions, to create an insulated liquid environment without ionic conductivity. Figures 3(a) and (b) show the PFM amplitude and phase images observed by the single-frequency mode at 130 kHz in decane, respectively. The phase contrast across the boundary is 170° $\pm$ 5°. The amplitude map is bisected by a clear domain boundary, corresponding to the characteristic minimum of amplitude at the *DW*.

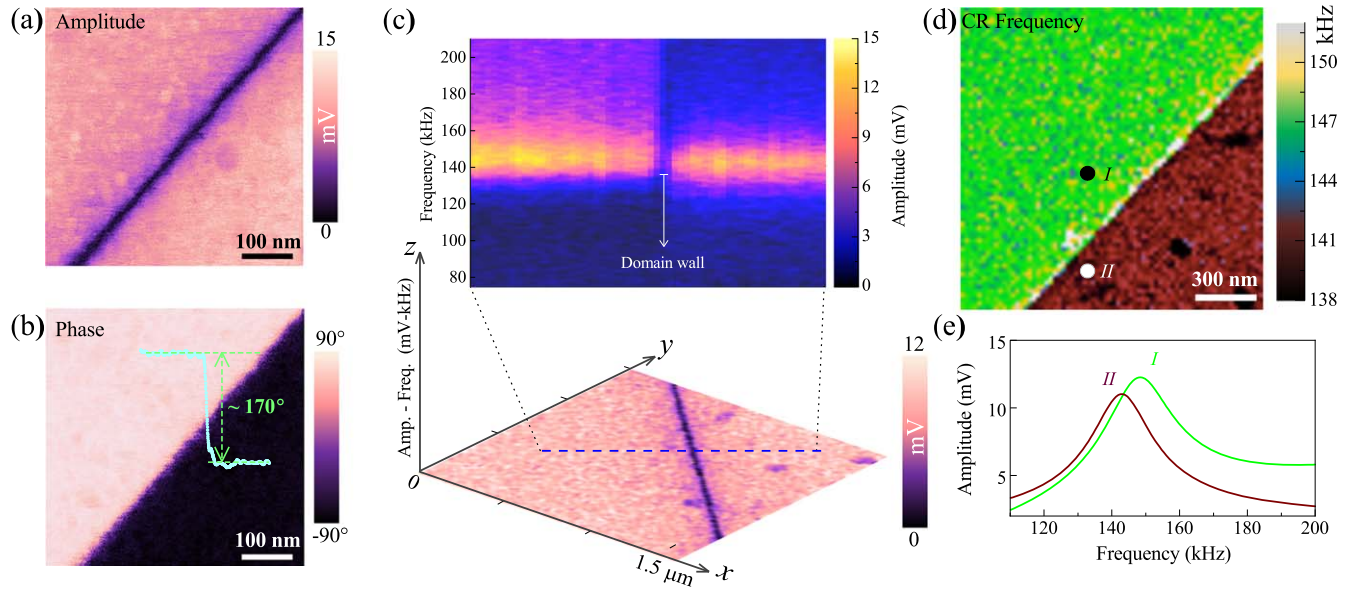

Figure 3. Electromechanical imaging in decane. (a) Amplitude and (b) phase images mapped via single-frequency PFM in decane. The line scan in (b) shows the phase contrast of about 170° across the antiparallel domains. By DCUBE-PFM, (c) three-dimensional amplitude cube imaged at the excitation frequency range from 75 to 210 kHz in non-polar decane. Line profile across the domain wall in CR amplitude image (Lower) corresponds to the frequency dependent amplitude response (Upper), which is along the z axis (Amp.–Freq. curves). The x–y plane presents the two-dimensional scanning area of 1.5 μm^2 with 72 × 72 pixels. (d) Fitted resonant frequency image and (e) the fitted spectra of contact resonace extracted from the corresponding marked domain regions I and II.

Three-dimensional piezoresponse amplitude was acquired with 72 × 72 pixels in the x–y plane by DCUBE-PFM in decane, as shown in figure 3(c). The amplitude responses $A(\omega)$ at the drive frequency range of 75–210 kHz were extracted as mapped in the upper panel, corresponding to the the dashed line in the lower panel. Ferroelectric domain boundary can be recognized with the wall size of less than three pixels. The CR phase in figure S2 (see the supporting information) was extracted at the resonant frequency of every pixel. The contrast of much less than 180° in CR phase is ascribed to that both phase responses of the adjacent domains turn to the reverse direction across the resonant frequency. Movie S3 displays the 3D frequency and location dependent amplitude image $\{A, \varphi\}(x, y, \omega)$ measured by DCUBE-PFM in decane. In opposite polarized structures marked as I and II in figures 3(d) and (e), the variation of resonant frequency is about 7 kHz. The various frequency curves present the different electromechanical responses between the domain I and II. The polarization dependence of piezoresponse would be attributed to the asymmetric lattice structure of PPLN under the poling process [37]. Experimental results confirm that the non-polar decane offers a comfortable environment to probe electromechanical effect with high resolution due to the elimination of the electrical field screening effect.

The visualization of electromechanical phenomena by PFM in polar solution is of higher interest. The striped domain of PPLN crystal has been mapped with high resolution in DI water. Figures 4(a) and (b) illustrate the amplitude and phase channels observed at the vicinity of contact resonance, 115 kHz, by traditional single-frequency PFM mode, where the performance of the electromechanical imaging in DI water can be comparable to that in air. The antiparallel-polarized domain was mapped with the great magnitude of piezoresponse and the reliable phase contrast of about 180° across the *DW*, where the amplitude magnitude reduces at the *DW*. Likewise, DCUBE-PFM mode characterizes the striped domains of PPLN pixel by pixel with more detailed information of cantilever behavior. Figure 4(c) shows the piezoresponse amplitude of ferroelectric domain observed at the CR frequency of each pixel. The CR frequency mapping in figure 4(d) indicates that the contact resonance of cantilever dynamic during electromechanical imaging is sensitive to the opposite domains. Even in the case of a low frame (16 × 16) array, the adjacent pixels across the *DW* could efficiently distinguish the varied piezoresponse with opposite polarization. At the same time, in order to detail the location (x, y) and frequency (ω) dependent piezoresponse $A(x, y, \omega)$ in DI water, we randomly choose a line scan (dashed line in figure 4(c)) to illustrate it as shown in figure 4(e). The resonance enhanced amplitude could be detected at the vicinity of the 120–130 kHz. Owing to the variations of CR amplitude and CR frequency on antiparallel domains, the mapping of frequency dependent piezoresponse could recognize the position of *DW* at the adjacent image pixels. Therefore, it is proven that the electromechanical imaging by using both traditional single-frequency PFM mode and DCUBE mode is permitted to acquire high resolution signals in DI water.

However, PFM mapping in electrolytes with higher ionic strength is challenging. The effect of electrolyte concentration has been observed with the molarity of NaCl solution increasing up to 10 mM. Figures S3, S4, and S5 in supporting information illustrate the piezoresponse amplitude and phase signals mapped by DCUBE-PFM at a range of frequencies in DI water and in NaCl solutions of 1 and 10 mM, respectively.

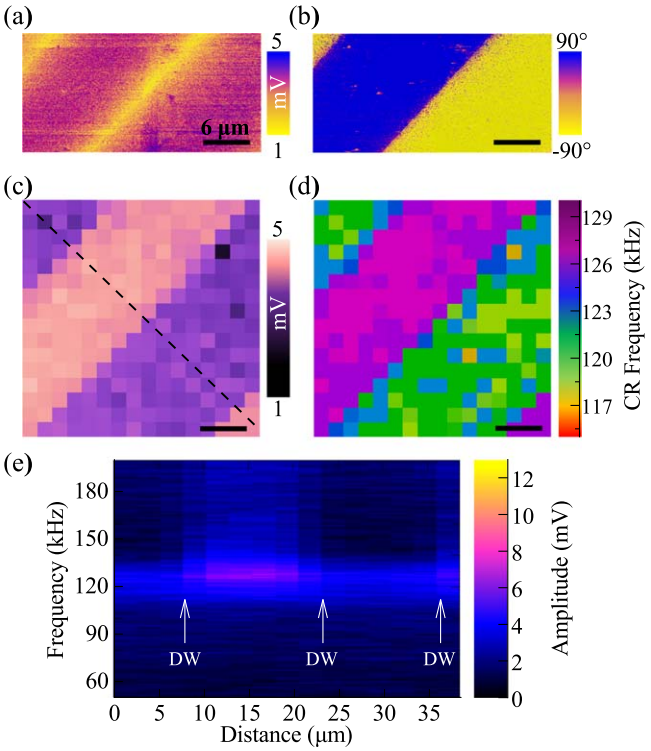

Figure 4. Electromechanical imaging in DI water. In DI water, (a) amplitude and (b) phase observed via single-frequency PFM at 115 kHz near contact resonance. The amplitude signal presents the good piezoresponse and the reduced response at the domain wall, while the excellent phase contrast illustrates the oppositely polarized orientation. By using DCUBE-PFM mode in DI water, (c) the CR amplitude and (d) the CR frequency with a mesh of 16 × 16 pixels. Despite the low frame of image, the adjacent domains could be distinguished clearly pixel by pixel. (e) Frequency dependent piezoresponse amplitude at different positions along the dashed line plotted in panel (c). This line profile crosses three domain walls (DW), as marked by the arrows.

With the drive frequency increasing to over 550 kHz, the measured amplitude and phase continuously change. As is shown, in DI water and NaCl solution of 1 mM, the good resolution of domain visualization can be obtained at many modulation frequencies, presenting the obvious phase contrast. However, figure S5 shows the ambiguous amplitude and phase distribution in NaCl solution of 10 mM, even though the weak signal could be observed in about 470, 482, and 502 kHz. In order to further quantify the variation of imaging ability in different environments, the optimal values of phase contrast, as the measurement criteria, have been summarized into figure 5. The phase contrast drops dramatically from about 180° to less than 30°, upon changing the media from DI water to NaCl solutions. The sharp drop of resolution in NaCl solutions with high ionic strength could be attributed to the strong screening effect around the tip-surface system [27]. In polar solutions, the presence and field-oriented drift of mobile ions complicate the implementation of electromechanical imaging. The ions undergo electromigration in response to the applied modulation field, forming electrical double layers (EDLs) that electrically

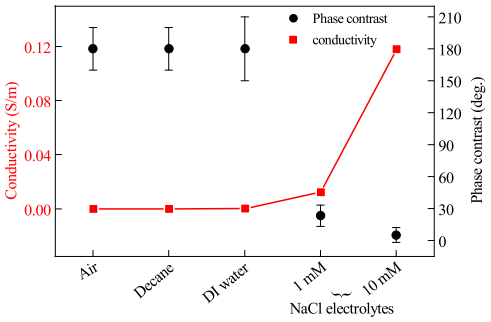

Figure 5. The observed phase contrast and conductivity in different environments. Ambient conductivity and the observed phase contrast in air, decane, DI water, and NaCl electrolytes of 1 and 10 mM.

screen the tip and charged ferroelectric surface. The details have been demonstrated as following.

3.3. Physical mechanism considerations

In order to clarify the effect of the electrolyte concentration, the field distribution across the EDL structure and the electrical interactions in the tip-sample junction have been shown schematically in figure 6. Good electrical interactions between tip and sample play an important role in electromechanical imaging. The long-range electrostatic and short-range electromechanical interactions coexist in contact mode of tip-sample system in ambient medium as referred to in figure 6(a). To some extent, the electrostatic force and the real size of the tip apex may restrict the spatial resolution of PFM signal. In polar solutions, the charged surface of sample and biased tip lead to the formation of EDLs, which consist of the Stern or Helmholtz layer and the adjacent diffuse layer based on the Gouy–Chapman–Stern model [38–40]. Both the Stern and diffuse layers can decay the electrical potential distribution along the normal direction of the tip or sample surface. During PFM imaging in polar liquids, we first assume that the tip touches the sample surface as close as the relative position like that in air, as shown in figure 6(b). Long-range electrostatic forces were screened by the formation of EDL structure. As marked by the thick double arrow in figure 6(b), the direct electromechanical coupling can be efficiently probed without the long-range electrostatic effect, where the effective working radius of tip is much less than that in air. However, plenty of experimental results confirm that high ionic strength of electrolyte has to bring the absence of PFM resolution owing to the strong field screening effect [27, 28]. Therefore, it could be claimed that the situation like the illustration in figure 6(b) is not applicable to the actual detection in highly conductive liquid environments.

In reality, a gap, or called ‘dead layer’, is always present between tip and sample surface during PFM working [28]. It is formed based on some factors including a low-polarized layer of surface adsorbates on the tip and sample, the opposite hydrophilic and hydrophobic properties between the metal tip apex and the sample, and the mismatch spatial dimension between the sample roughness and tip radius. The size of the gap is generally on the order of several nanometers. Figure 6(c)

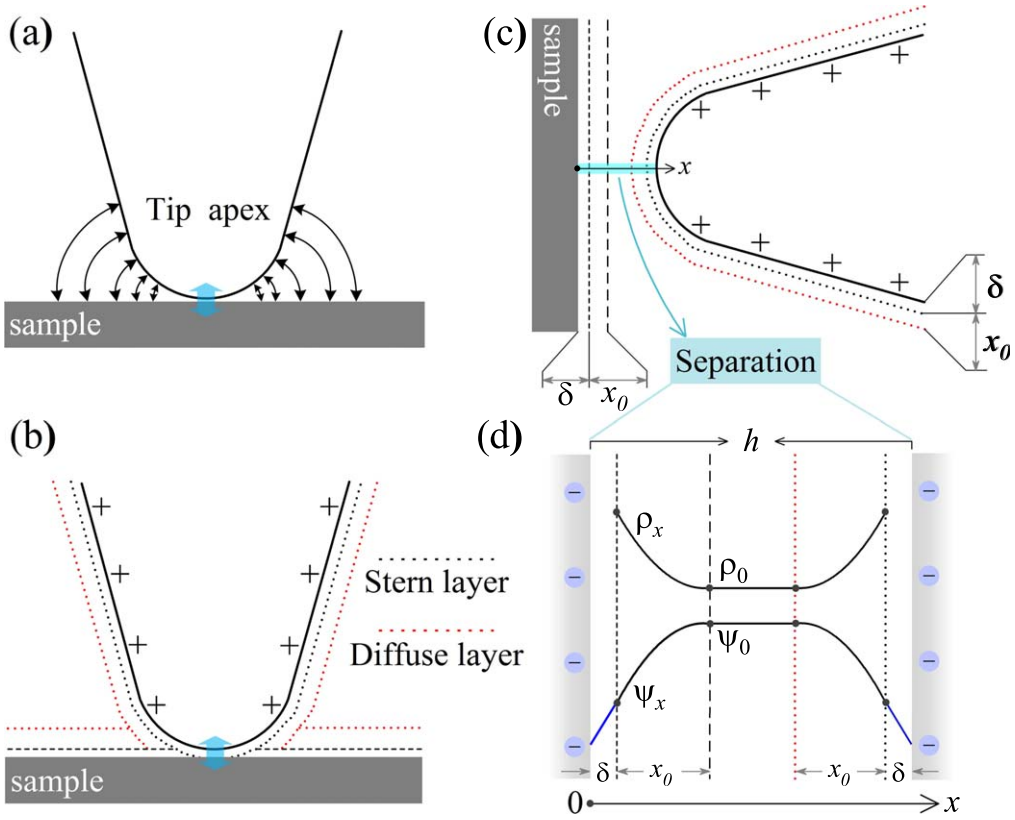

Figure 6. Schematic models of the electrical interactions and field behavior between tip and sample surface. (a) Electromechanical and electrostatic interactions in the tip-sample junction in air. Electromechanical coupling, as marked by the thick blue double-arrow, is present only when tip and surface are in contact. In polar liquids, the double layer structure in tip-surface junction are shown when tip and surface are in (b) contact and (c) non-contact states, respectively. For delineating the outline of EDLs structure, the dashed lines represent the compact Stern layer (red) and the diffuse layer (black), respectively. (d) The counterion density profile ρ_x and electrical potential ψ_x distribution along x direction are schematically present corresponding to the tip-surface separation shown as the narrow rectangle area in panel (c), where the distance between two negatively charged surfaces is assumed as $h > 2(\delta + x_0)$.

shows the fixed separation, considered as the dead layer, between tip and sample surface. If the width of this separation is more than one whole EDL structure, the potential distribution across EDL structure may dominate the electrical interactions between the tip and sample. The scale of EDL structure is quantified in the thickness of the Stern layer, δ and that of the diffuse layer, x_0. In order to clearly clarify the field screening effect in this gap of tip-surface junction, the ion density profile (ρ_x, mol l^{-1}) and electrical potential distribution (ψ_x, V) have been schematically presented along the x direction in figure 6(d). Double identical negative-charged surfaces are considered as the representatives of tip and sample surface, where the separation (distance: h) is more than twice as thick as one EDL structure, $h > 2(\delta + x_0)$. It is assumed that no other specifically adsorbed ion is presented at the interfaces in the ideal case. Since only potential differences are ever physically valuable, we have set the bulk potential $\psi_0 = 0$ far away from the charged surface, where the bulk concentration is n_0, the counterion density of bulk $\rho = \rho_0$, and the electric field $E = -\frac{\partial \psi}{\partial x} = 0$ by symmetry at the bulk solution. The fully or partially hydrated cations congregate in a large number at the vicinity of the negatively charged surface.

The Stern layer is mainly filled with water molecules and can be modeled as a plane parallel capacitor, corresponding to the linear drop of the potential ψ in figure 6(d). The locus of the electrical centers of the nearest hydrated counterions is regarded as the outer Helmholtz plane (OHP). For the case when only counterions exist in solution, the ionic distribution and electrical field behavior within the diffuse layer obey equation (3) and the Poisson–Boltzmann equation (4) as follows, respectively

$$\rho(x) = \rho_0 \exp\left(\frac{-ze\psi(x)}{k_B T}\right), \tag{3}$$

$$\frac{\partial^2 \psi}{\partial x^2} = \frac{-zen_0}{\varepsilon_0 \varepsilon_r} \exp\left(\frac{-ze\psi(x)}{k_B T}\right), \tag{4}$$

where z is the solute valency, $\varepsilon_r \varepsilon_0$ is the dielectric constant, k_B is the Boltzmann constant, T is the absolute temperature, and e is the elementary charge, respectively [38, 40]. The diffuse layer extends from the OHP to the bulk of the electrolyte solution, where the corresponding thickness is marked as x_0. Note that both $\rho(x)$ and $\psi(x)$ profiles present an exponential evolution. In electrolytes, most of the hydrated counterions that could efficiently balance the surface charge are gathered within a sub-nanometer distance from the surface. It can be seen that the characteristic distribution distance ($\delta + x_0$) of EDL structure is determined by the sum of δ and the Debye length λ_D, where the latter depends solely on the bulk

molarity of solution. For a monovalent 1:1 electrolyte at 298 K, $\lambda_D = \sqrt{(\varepsilon_0 \varepsilon_r k_B T / 2 n_0 e^2)} \approx 0.304 / \sqrt{n_0}$ nm. The Debye length λ_D is about 3.04 nm, 9.6 nm for NaCl solutions of 10 mM, 1 mM and 960 nm for DI water, respectively. Within the scale of $(\delta + \lambda_D)$, both the absolute values of ionic density $|\rho(x)|$ and electrical potential $|\psi(x)|$ gradually decrease crossing the Stern and diffuse layers from the tip and sample surfaces. The outer area of EDL, $x > (\delta + x_0)$, is considered as the zero-potential distribution. Hence, EDL structure could shield the electrical potential in the range of $(\delta + x_0)$. If the gap between tip and surface can accommodate the whole EDL structure, the effective electrical interactions involving the electromechanical coupling will be greatly shielded, as called field screening effect. In our results, when the bulk concentration is over 1 mM in NaCl solutions, the Debye length λ_D is less than 9.6 nm. Therefore, the precipitous reduction of electrical interaction in the gap between the tip and sample leads to the bad performance in PFM imaging. In other words, the electromechanical interactions between the tip and sample were screened by the appearance of EDL structure in the dead gap.

The *ac* bias with the appropriate frequency is applied as excitation signals for the electromechanical probing, where the frequency is generally set within the range of 10–10^3 kHz. The discussions about the Debye screening effect mentioned above are based on the time-invariant state holding the homeostatic potentials for both the tip and sample surfaces. However, the time-resolved field distribution in the tip-sample system under the ionic dynamics is another key point of concern about the effect on the imaging resolution of the voltage-modulated SPM. The Debye time, $\tau_D = \lambda_D^2 / D$, indicates the time of the ionic diffusion crossing the EDL, where D is the ionic diffusivity across one Debye screening length. Generally, the Debye time τ_D is in the range of nano to micro seconds (ns–μs) [41, 42]. Some simulation results, based on the modified Poisson–Nernst–Plank model [43], have revealed the correlations between the modulated frequency, the ion concentration of the polar solution and the effect of ionic dynamics at the tip-surface junction [42]. At the lower frequency range, the electrical behaviors are dominated by the presence of the Faradic processes and the ionic electromigration, where the electrochemical effects could be efficiently controlled and explored in this case.

The ideal static equilibrium of ionic motion in a conductive liquid environment is beneficial to the electromechanical interaction between the tip and sample surface. However, the study of electromechanical detections in liquid media via PFM focuses on the solution molarity ranges of over 10^{-4} M under the effective frequency space of 10^3–10^6 Hz. On this occasion, the field-oriented ion dynamics leads to the Debye screening effect as systematically discussed in figure 6. For example, when the drive frequency is over 10^4 Hz, the mobile ions around the tip-surface system in distilled water are in quasi-static equilibrium [42]. Currently, the accessible frequency range in commercial SPM systems is usually from *dc* to 10^7 Hz. However, it requires a frequency of more than 10^7 Hz to reach the quasi-static equilibrium for testing in the polar solutions of over 10^{-3} M. In view of the time-variant field distribution, a series of further experimental investigations will be worth carrying out for improving the spatial resolution of PFM imaging in highly conductive liquid environments. In order to avoid the electrical field screening effect in the liquid PFM measurements, we think that some possible approaches, such as macroscopic field-induced ion dynamics, the modifications of the tip-sample junction and the ionic exchange by the Faradic process, may be helpful in future studies.

4. Conclusion

We have proposed the DCUBE-PFM mode to visualize electromechanical phenomena and elucidated the relative physical mechanisms for electromechanical imaging in liquid environments. DCUBE-PFM technique, as similar with the typical dual ac resonance tracking or band excitation PFM mode [15, 16], could improve the imaging quality of the resonance enhanced piezoresponse. Besides, DCUBE-PFM introduced the unique FFV method to realize the detection of materials' mechanical property in the intermittent contact mode. In ambient and liquid environments, three-dimensional electromechanical and mechanical information can be synchronously acquired on the nanoscale. The high-resolution ferroelectric domain with the phase contrast of 180° between antiparallel domains of a PPLN sample were achieved in both decane and DI water by the single-frequency PFM and DCUBE-PFM imaged at a wide frequency range. Detailed theoretical discussions accompanied by the experimental results have indicated the time-invariant Debye field screening effect from the ionic electromigration in the tip-sample junction on the basis of the Gouy–Chapman–Stern model. Additionally, we considered the time-resolved effect on the electromechanical imaging in polar solutions, which clarified the relations among the modulated frequency, the solution molarity and the ion dynamics. The investigations are of high interest for (i) developing PFM technique based on big data analysis and processing, (ii) improving the resolution of electromechanical imaging in high-concentration electrolytes or *in vivo* body fluids, as well as (iii) efficiently probing the weak piezoelectricity of electromechanical systems.

Acknowledgments

This work was financially supported by National Key Research and Development Program of China (grant no. 2018YFB0406500), Natural Science Foundation of China (grant nos. 61674057 and 61227902), Projects of Science and Technology Commission of Shanghai Municipality (grant nos. 18JC1412400, 18YF1407200, and 18YF1407000), and the Program for Professor of Special Appointment (Eastern Scholar) at Shanghai Institutions of Higher Learning and the Fundamental Research Funds for the Central Universities.

ORCID iDs

Zhigao Hu https://orcid.org/0000-0003-0575-2191

References

[1] Kolosov O, Gruverman A, Hatano J, Takahashi K and Tokumoto H 1995 Nanoscale visualization and control of ferroelectric domains by atomic force microscopy *Phys. Rev. Lett.* **74** 4309

[2] Cui A Y, Jiang K, Zhang P, Xu L P, Xu G S, Chen X M, Hu Z G and Chu J H 2017 *In situ* exploration of thermal-induced domain evolution with phase transition in $LiNbO_3$-modified $K_{0.5}Na_{0.5}NbO_3$ single crystal *J. Phys. Chem.* C **121** 14322

[3] Lee B Y, Zhang J, Zueger C, Chung W J, Yoo S Y, Wang E, Meyer J, Ramesh R and Lee S W 2012 Virus-based piezoelectric energy generation *Nat. Nanotechnol.* **7** 351

[4] Li T, Chen L and Zeng K 2013 *In situ* studies of nanoscale electromechanical behavior of nacre under flexual stresses using excitation PFM *Acta Biomater.* **9** 5903

[5] Jiang P, Yan F, Nasr Esfahani E, Xie S, Zou D, Liu X, Zheng H and Li J 2017 Electromechanical coupling of murine lung tissues probed by piezoresponse force microscopy *ACS Biomater. Sci. Eng.* **3** 1827

[6] Nguyen T D, Deshmukh N, Nagarah J M, Kramer T, Purohit P K, Berry M J and McAlpine M C 2012 Piezoelectric nanoribbons for monitoring cellular deformations *Nat. Nanotechnol.* **7** 587

[7] Kepler R G and Anderson R A 1992 Ferroelectric polymers *Adv. Phys.* **41** 1

[8] Nellist M R, Laskowski F A L, Qiu J, Hajibabaei H, Sivula K, Hamann T W and Boettcher S W 2017 Potential-sensing electrochemical atomic force microscopy for in operando analysis of water-splitting catalysts and interfaces *Nat. Energy* **3** 46

[9] Nazri G A and Pistoia G 2009 *Eds. Lithium Batteries: Science and Technology* (New York: Springer)

[10] Adler S 2004 Factors governing oxygen reduction in solid oxide fuel cell cathodes *Chem. Rev.* **104** 4791

[11] Wu W *et al* 2014 Piezoelectricity of single-atomic-layer MoS_2 for energy conversion and piezotronics *Nature* **514** 470

[12] Duerloo K-A N, Ong M T and Reed E J 2012 Intrinsic piezoelectricity in two-dimensional materials *J. Phys. Chem. Lett.* **3** 2871

[13] Okino H, Sakamoto J and Yamamoto T 2003 Contact-resonance piezoresponse force microscope and its application to domain observation of $Pb(Mg_{1/3}Nb_{2/3})O_3$–$PbTiO_3$ single crystals *Japan. J. Appl. Phys.* **42** 6209

[14] Bradler S, Kachel S R, Schirmeisen A and Roling B 2016 A theoretical model for the cantilever motion in contact-resonance atomic force microscopy and its application to phase calibration in piezoresponse force and electrochemical strain microscopy *J. Appl. Phys.* **120** 165107

[15] Rodriguez B J, Callahan C, Kalinin S V and Proksch R 2007 Dual-frequency resonance-tracking atomic force microscopy *Nanotechnology* **18** 475504

[16] Jesse S, Kalinin S V, Proksch R, Baddorf A P and Rodriguez B J 2007 The band excitation method in scanning probe microscopy for rapid mapping of energy dissipation on the nanoscale *Nanotechnology* **18** 435503

[17] Rodriguez B J, Jesse S, Habelitz S, Proksch R and Kalinin S V 2009 Intermittent contact mode piezoresponse force microscopy in a liquid environment *Nanotechnology* **20** 195701

[18] Jesse S, Mirman B and Kalinin S V 2006 Resonance enhancement in piezoresponse force microscopy: mapping electromechanical activity, contact stiffness, and *Q* factor *Appl. Phys. Lett.* **89** 022906

[19] Calahorra Y, Smith M, Datta A, Benisty H and Kar-Narayan S 2017 Mapping piezoelectric response in nanomaterials using a dedicated non-destructive scanning probe technique *Nanoscale* **9** 19290

[20] Kalinin A, Atepalikhin V, Pakhomov O, Kholkin A L and Tselev A 2018 An atomic force microscopy mode for nondestructive electromechanical studies and its application to diphenylalanine peptide nanotubes *Ultramicroscopy* **185** 49

[21] Kalinin S V, Sumpter B G and Archibald R K 2015 Big-deep-smart data in imaging for guiding materials design *Nat. Mater.* **14** 973

[22] Kalinin S V *et al* 2016 Big, deep, and smart data in scanning probe microscopy *ACS Nano* **10** 9068

[23] Dcikey E and Arthor G 2017 Big data meets materials science: training the future generation *Am. Ceram. Soc. Bull.* **96** 42–7 (https://bulletin-archive.ceramics.org/ucukbm.pdf)

[24] Belianinov A, Kalinin S V and Jesse S 2015 Complete information acquisition in dynamic force microscopy *Nat. Commun.* **6** 6550

[25] Umeda K, Kobayashi K, Oyabu N, Hirata Y, Matsushige K and Yamada H 2014 Practical aspects of Kelvin-probe force microscopy at solid/liquid interfaces in various liquid media *J. Appl. Phys.* **116** 134307

[26] Umeda K, Kobayashi K, Oyabu N, Matsushige K and Yamada H 2015 Molecular-scale quantitative charge density measurement of biological molecule by frequency modulation atomic force microscopy in aqueous solutions *Nanotechnology* **26** 285103

[27] Rodriguez B J, Jesse S, Baddorf A P and Kalinin S V 2006 High resolution electromechanical imaging of ferroelectric materials in a liquid environment by piezoresponse force microscopy *Phys. Rev. Lett.* **96** 237602

[28] Balke N, Tselev A, Arruda T M, Jesse S, Chu Y H and Kalinin S V 2012 Probing local electromechanical effects in highly conductive electrolytes *ACS Nano* **6** 10139

[29] Balke N, Jesse S, Chu Y H and Kalinin S V 2012 High-frequency electromechanical imaging of ferroelectrics in a liquid environment *ACS Nano* **6** 5559

[30] Kalinin S V, Rodriguez B J, Seal K, Proksch R, Jesse S, Hohlbauch S, Revenko I, Thompson G L and Vertegel A 2007 Towards local electromechanical probing of cellular and biomolecular systems in a liquid environment *Nanotechnology* **18** 424020

[31] Ramachandran P and Varoquaux G 2011 Mayavi: 3D visualization of scientific data *IEEE Comput. Sci. Eng.* **13** 40

[32] Alexe M and Gruverman A (ed) 2004 *Nanoscale Characterization of Ferroelectric Materials* (Berlin: Springer)

[33] Kalinin S V, Rodriguez B J, Jesse S, Karapetian E, Mirman B, Eliseev E A and Morozovska A N 2007 Nanoscale electromechanics of ferroelectric and biological systems: a new dimension in scanning probe microscopy *Annu. Rev. Mater. Res.* **37** 189

[34] Xie S, Gannepalli A, Chen Q N, Liu Y, Zhou Y, Proksch R and Li J 2012 High resolution quantitative piezoresponse force microscopy of $BiFeO_3$ nanofibers with dramatically enhanced sensitivity *Nanoscale* **4** 408

[35] Albrecht T R, Grütter P, Horne D and Rugar D 1991 Frequency modulation detection using high-*Q* cantilevers for enhanced force microscope sensitivity *J. Appl. Phys.* **69** 668

[36] Kholkin A, Kalinin S V, Roelofs A and Gruverman A 2007 Review of ferroelectric domain imaging by piezoresponse

force microscopy *Scanning Probe Microscopy* ed S Kalinin and A Gruverman (New York: Springer)
[37] Simone S and Wolf G S 2017 $LiNbO_3$ surfaces from a microscopic perspective *J. Phys.: Condens. Matter* **29** 413001
[38] Israelachvili J N 2011 *Intermolecular and Surface Forces* (Singapore: Elsevier) ch 14
[39] Ferris R J, Lin S, Therezien M, Yellen B B and Zauscher S 2013 Electric double layer formed by polarized ferroelectric thin films *ACS Appl. Mater. Interfaces* **5** 2610
[40] Bard A J and Faulkner L R 2000 *Electrochemical Methods: Fundamentals and Applications* (New York: Wiley) ch 1 and 13
[41] Bazant M Z, Thornton K and Ajdari A 2004 Diffuse-charge dynamics in electrochemical systems *Phys. Rev.* E **70** 021506
[42] Collins L *et al* 2014 Probing charge screening dynamics and electrochemical processes at the solid–liquid interface with electrochemical force microscopy *Nat. Commun.* **5** 3871
[43] Kilic M S, Bazant M Z and Ajdari A 2007 Steric effects in the dynamics of electrolytes at large applied voltages: I. Double-layer charging *Phys. Rev.* E **75** 021502
Kilic M S, Bazant M Z and Ajdari A 2007 Steric effects in the dynamics of electrolytes at large applied voltages: II. Modified Poisson–Nernst–Planck equations *Phys. Rev.* E **75** 021503